Scientific Research Publishing

Journal of Electromagnetic Analysis and Applications, 2026, 18(7), 113-140
https://www.scirp.org/journal/jemaa
ISSN Online: 1942-0749
ISSN Print: 1942-0730

An Industrial Standard in Weak Magnetic Field Sensing: A Comprehensive Review of KMZ51 Amr Sensor from Theory to Application

Huseyin Gunes[1], Burak Ege[2], Hakan Citak[3], Mustafa Coramik[4], Sabri Bicakci[5], Yavuz Ege[4]

[1]Department of Computer Engineering, Faculty of Engineering, Balikesir University, Balikesir, Türkiye
[2]Institute of Science, Balikesir University, Balikesir, Türkiye
[3]Balikesir Vocational High School, Balikesir University, Balikesir, Türkiye
[4]Department of Physics, Necatibey Faculty of Education, Balikesir University, Balikesir, Türkiye
[5]Department of Electric and Electronics Engineering, Faculty of Engineering, Balikesir University, Balikesir, Türkiye
Email: hgunes@balikesir.edu.tr, 202512605007@baun.edu.tr, hcitak@balikesir.edu.tr, mustafacoramik@balikesir.edu.tr, sbicakci@balikesir.edu.tr, yege@balikesir.edu.tr

How to cite this paper: Gunes, H., Ege, B., Citak, H., Coramik, M., Bicakci, S. and Ege, Y. (2026) An Industrial Standard in Weak Magnetic Field Sensing: A Comprehensive Review of KMZ51 Amr Sensor from Theory to Application. *Journal of Electromagnetic Analysis and Applications*, **18**, 113-140.
https://doi.org/10.4236/jemaa.2026.187007

Received: June 22, 2026
Accepted: July 28, 2026
Published: July 31, 2026

Abstract

Anisotropic Magnetoresistive (AMR) technology stands as one of the most prominent magnetic sensing methods, enabling the measurement of low-level magnetic fields with high sensitivity. Based on the direction-dependent resistance change observed in ferromagnetic materials, this technology is extensively utilized in navigation, automotive systems, industrial automation, space technologies, and non-destructive testing applications. Today, AMR-based sensors hold a critical intermediate position between Hall-effect and fluxgate sensors due to their low power consumption, high accuracy, and compact structures. The fundamental mechanism of the AMR effect relies on electron scattering processes, which vary depending on the angle between the current direction and the magnetization vector. This characteristic facilitates the measurement of weak magnetic fields, comparable to the Earth's magnetic field, at microtesla and nanotesla levels. In this study, the KMZ51 magnetic field sensor, widely recognized as one of the most mature and commercially successful embodiments of AMR technology, is comprehensively reviewed from theory to application. The KMZ51 is a high-sensitivity sensing device comprising a thin-film permalloy-based magnetoresistive Wheatstone bridge, an internal set/reset (flipping) coil, and a compensation coil. This paper details the physical foundations of the sensor, including Stoner-Wohlfarth energy models, Barber-Pole linearization geometry, and Wheatstone bridge mathematical derivations. Furthermore, fundamental field-level error sources such as temperature drift, cross-axis sensitivity, and hysteresis are investigated through mathematical models, and corresponding closed-loop feedback and synchronous lock-in detection circuit architectures are presented. A comprehensive performance matrix is established to benchmark the KMZ51 against alternative technologies such as GMR, TMR, and fluxgate sensors. Its functional roles in small-satellite Attitude Determination and Control Systems (ADCS), non-destructive testing via Magnetic Flux Leakage (MFL), and contactless current measurement systems for smart grids are also evaluated. In conclusion, this review demonstrates that although modern TMR sensors achieve higher absolute sensitivity levels, the KMZ51 maintains its standard in both research laboratories and field applications owing to its linear output characteristics, low 1/f noise, cost-effectiveness, and industrial reliability. It is projected that through MEMS integration, IoT-based sensor networks, and artificial intelligence-driven noise filtering algorithms, AMR sensors will continue to play an integral role in highly advanced autonomous platforms in the future.

Keywords

Anisotropic Magnetoresistance (AMR), KMZ51, Magnetic Field Sensor, Magnetometer, Electronic Compass, Traffic Detection, Non-Destructive Testing (NDT)

1. Introduction

1.1. Historical Evolution of Magnetic Field Sensors

Magnetic field sensors currently possess a vast array of applications ranging from scientific research to industrial automation. While early magnetic measurement systems comprised bulky electromechanical structures, the advancement of semiconductor and thin-film technologies has led to the development of smaller, more sensitive, and cost-effective sensors [1]. In particular, rapid developments in automotive electronics, robotic systems, defense applications, and consumer electronics have driven an ever-increasing demand for high-performance magnetic sensing devices [2] [3].

For many years, Hall-effect sensors remained the most widely utilized magnetic field sensors. Although their simplistic structure and low cost offer significant advantages, they exhibit limited sensitivity and high offset drift at low-level magnetic fields (*i.e.*, on the order of the Earth's magnetic field). Conversely, while fluxgate sensors provide exceptionally high sensitivity, their complex driving circuitry, large volumetric size, and substantial power consumption render them unsuitable for portable devices or microsystem applications [1] [4].

As a consequence of these technological limitations, magnetoresistive sensor technologies emerged. In particular, Anisotropic Magnetoresistance (AMR), Giant Magnetoresistance (GMR), and Tunnel Magnetoresistance (TMR) sensors have undergone significant advancements over the last three decades. Among these, AMR sensors are extensively utilized in weak magnetic field measurements owing to their high sensitivity, low power consumption, compatibility with monolithic integration, and compact dimensions. Today, AMR sensors occupy a prominent position in navigation systems, electronic compasses, traffic detection systems, non-destructive testing, and current sensing applications [5] [6].

1.2. Significance of AMR Sensors

The Anisotropic Magnetoresistance effect is predicated on the principle that the electrical resistance of ferromagnetic materials varies depending on the direction of their magnetization [7]. Through this effect, extremely minute fluctuations in magnetic fields can be transduced into electrical signals. AMR sensors offer approximately 10 to 50 times higher sensitivity compared to Hall-effect sensors and exhibit a superior signal-to-noise ratio (SNR), particularly in low-level magnetic field measurements [8].

The primary advantages of AMR sensors can be summarized as follows:

- High sensitivity and resolution (nanotesla order)
- Low power consumption (milliwatt level)
- Compact, monolithic thin-film structure
- Cost-effectiveness and mature manufacturing technology
- High reliability and solid-state robustness
- Wide operating temperature range (from −40˚C to +125˚C)
- Facilitated calibration and zero-field operation via internal coils

Owing to these definitive advantages, AMR technology has been preferred in industrial applications for many years. In particular, the KMZ sensor series, originally developed by Philips (currently NXP), stands among the most commercially successful embodiments of AMR technology that have evolved into a global standard based on specific criteria including its highly linear output, internal compensation features, extensive documented field use, and competitive cost-to-performance ratio [9] [10].

1.3. Scope of the Study

The primary objective of this comprehensive review is to systematically examine the operating principles, structural characteristics, error models, signal conditioning topologies, and contemporary application domains of KMZ51-based AMR sensors. This study initially elucidates the physical foundations and mathematical models of the AMR effect, followed by an in-depth analysis of the Barber-Pole geometry, Wheatstone bridge mathematical derivations, and electrical parameters inherent to the KMZ51 sensor. Subsequently, fundamental field-level error sources, namely temperature drift, cross-axis sensitivity, and hysteresis, are formulated through mathematical models and closed-loop synchronous detection circuit architectures are investigated. In the concluding sections, a comparative performance matrix is established to benchmark the KMZ51 against alternative GMR, TMR, and fluxgate technologies, prominent experimental studies in the literature are summarized, and advanced technological application domains such as space systems, Non-Destructive Testing (NDT), and smart grids are discussed.

1.4. Literature Review Methodology

The literature discussed throughout this review, particularly the applied studies and research outcomes analyzed in Sections 7 and 8, was selected through systematic searches in academic databases including IEEE Xplore, ScienceDirect, and Scopus. While foundational physics and sensor specifications were sourced from established textbooks and manufacturer datasheets, the modern application literature was identified using primary search terms such as "KMZ51", "AMR sensor applications", and "anisotropic magnetoresistance". The inclusion criteria for the application sections focused on peer-reviewed journal articles and conference proceedings published within the last three decades that explicitly demonstrated the field application, signal conditioning, or performance benchmarking of the KMZ51 sensor.

2. Anisotropic Magnetoresistance (AMR) Effect and Physical Foundations

2.1. Historical Development

The Anisotropic Magnetoresistance effect was first discovered in 1856 by William Thomson (Lord Kelvin) [11]. Thomson demonstrated that the electrical resistance of ferromagnetic materials, such as iron and nickel, varies depending on the direction of an applied external magnetic field. This discovery is recognized as the foundational observation underpinning modern magnetoresistive sensors [12].

For many years, the precise physical mechanism of the AMR effect remained incompletely understood. Subsequent studies revealed that spin-orbit interactions and s-d band electron scattering processes in 3 d ferromagnetic transition metals constitute the fundamental cause of this phenomenon [13]. Furthermore, the evolution of photolithography and thin-film vacuum deposition technologies, particularly during the second half of the 20th century, enabled the realization of commercial AMR sensors in integrated circuit (IC) format [5] [14].

2.2. Classification and Mathematical Definition of Magnetoresistance

The Magnetoresistive (MR) effect is predicated on the fundamental principle that the electrical resistance of a conducting or semiconducting material alters in the presence of an external magnetic field. The magnitude of the MR effect is quantified by a dimensionless ratio and is expressed by the following equation, which depends on the physical characteristics of the material from which the conductor is fabricated:

$$M_R = \frac{\rho_B - \rho_0}{\rho_0} \times 100\% \tag{1}$$

In Equation (1), ρ_B denotes the resistivity (Ω·m) of the conductor in the presence of an arbitrary magnetic field B, whereas ρ_0 represents its resistivity in the absence of an applied magnetic field [14]. Depending on material architecture and quantum scattering mechanisms, MR effects can be categorized as follows:

- Ordinary Magnetoresistance (OMR): Observed in non-magnetic conducting metals due to the influence of the Lorentz force.
- Anisotropic Magnetoresistance (AMR): Arises in ferromagnetic alloys as a consequence of spin-orbit interaction.
- Giant Magnetoresistance (GMR): Occurs via spin-dependent scattering in superlattice structures comprising alternating ferromagnetic alloy layers and conductive metallic interlayers (e.g., Fe/Cr).
- Tunneling Magnetoresistance (TMR): Realized in Magnetic Tunnel Junctions (MTJs) consisting of multiple ferromagnetic alloy layers separated by a thin insulating barrier (e.g., MgO or Al_2O_3).
- Ballistic Magnetoresistance (BMR): Occurs in architectures featuring multilayer ferromagnetic alloys separated by non-ferromagnetic nanodot contacts.

Colossal Magnetoresistance (CMR): Observed in perovskite manganite structures $A_{1-x}B_xMnO_3$, where A = La, Pr, Nd or Sm; or B = Ca, Sr or Ba driven by strong electron-phonon interactions.

2.3. Permalloy Thin-Film Physics and Easy Axis

When examining a thin film fabricated from a ferromagnetic material, specifically the $Ni_{81}Fe_{19}$ Permalloy alloy, which comprises 81% nickel and 19% iron, a strong external magnetic field is applied parallel to the x-axis during the deposition process (Figure 1). This magnetic field, which is removed once the deposition is complete and the film has cooled, establishes a uniaxial residual magnetic anisotropy in the +x direction, termed the "easy axis" of the film [15]. Since the film is inherently a ferromagnetic material, the magnetic domains retain this easy-axis orientation when the external field is zero [16].

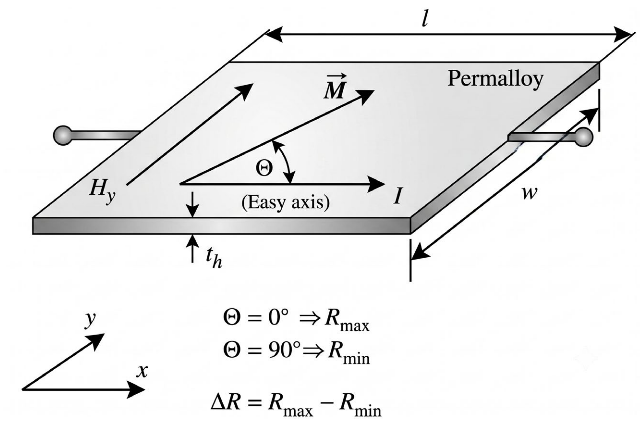

Figure 1. Application of a magnetic field onto a current-carrying permalloy film.

If no external magnetic field is applied to the film, the resultant magnetization vector ($\boldsymbol{M}$) remains aligned with the easy axis. Consequently, the angle Θ, defined between the vector $\boldsymbol{M}$ and the current passing through the film (in the +x direction), evaluates to zero (Θ = 0˚). Under this condition, the resistance of the sensor (R) attains its maximum value, R_{max}. Conversely, if an external magnetic field of magnitude H_y acts upon the film in the $+y$ direction, the resultant magnetization vector $\boldsymbol{M}$ is influenced, causing the angle Θ to deviate from zero. If the magnetic field H_y is sufficiently strong, it can rotate the vector $\boldsymbol{M}$ until it is almost completely parallel to the field ($\Theta \approx 90^{\circ}$). In this scenario, the resistance R reaches its minimum value, R_{min}. Therefore, the angle Θ is directly correlated with the magnitude of the magnetic field H_y [5] [16]-[19].

The dependence of the sensor resistance R on the angle Θ is generally expressed by the following formulation:

$$R(\Theta) = \rho_{\perp}\frac{l}{wt_h} + \left(\rho_{/\!/} - \rho_{\perp}\right)\frac{l}{wt_h}\cos^2(\Theta) \tag{2}$$

Here, the quantities denoted by $\rho_{\perp}$ and $\rho_{/\!/}$ represent the resistivities when the magnetization vector $\boldsymbol{M}$ is perpendicular and parallel to the current (and the easy axis), respectively. The parameters l, w, and t_h designate the length, width, and thickness of the film, respectively (typically involving sub-micrometer geometries where $l > w \gg t_h$) [15]. Rearranging Equation (2) yields:

$$R(\Theta) = R_0 + \left(R_{max} - R_{min}\right)\cos^2(\Theta) \tag{3}$$

The resistance R_0 (or R_{min}) corresponds to the baseline resistance value that emerges when the magnetization vector $\boldsymbol{M}$ is perpendicular to the current flow. Finally, Equation (3) can be expressed in a more simplified form as [17]:

$$R(\Theta) = R_0 + \Delta R \cdot \cos^2(\Theta) \tag{4}$$

The values of R_0 and ΔR vary depending on the resistivity coefficients of the material and the strip geometry; for permalloy, ΔR is approximately 2% to 3% of the baseline value R_0 [16]. Furthermore, by performing the necessary mathematical rearrangements on Equation (3) and utilizing the identity $R_0 = R_{min}$, the following alternative trigonometric expansions can be derived:

$$R(\Theta) = R_{max}\cos^2(\Theta) + R_{min} - R_{min}\cos^2(\Theta) \tag{5}$$

$$R(\Theta) = R_{max}\cos^2(\Theta) + R_{min}\left(1 - \cos^2(\Theta)\right) \tag{6}$$

$$R(\Theta) = R_{max}\cos^2(\Theta) + R_{min}\sin^2(\Theta) \tag{7}$$

Letting H_{max} denote the maximum magnetic field value that the AMR sensor can detect before reaching saturation, the relationship between the angle Θ and the field H_y is governed by the following equalities [15]:

$$\cos^2(\Theta) = 1 - \left(\frac{H_y}{H_{max}}\right)^2 \quad \text{ve} \quad \sin^2(\Theta) = \left(\frac{H_y}{H_{max}}\right)^2 \tag{8}$$

When the external magnetic field H_y reaches a magnitude sufficient to completely rotate the magnetization vector $\boldsymbol{M}$ toward itself (*i.e.*, as H_y to H_{max}), the angle Θ approaches 90°. Consequently, the resistance equation can be expressed as [15]:

$$R(H_y) = R_0 + \left(R_{max} - R_{min}\right)\left[1 - \left(\frac{H_y}{H_{max}}\right)^2\right] \quad \left(H_y \le H_{max}\right) \tag{9}$$

For the saturating condition where $H_y > H_{max}$, the resistance R reaches saturation and remains constant at its minimum baseline value, R_0.

2.4. Energy Equations and Anisotropy Field

Consider a scenario where the applied magnetic field vector H is not constrained solely along the y-axis but possesses both H_x and H_y components. In such a system, the total free energy of a single-domain ferromagnetic film exhibiting magnetoresistive properties under an applied magnetic field (Stoner-Wohlfarth model) can be expressed as the sum of the magnetostatic Zeeman energy (E_{mag}) and the uniaxial anisotropy energy (E_{an}):

$$E = E_{mag} + E_{an} \tag{10}$$

Letting K_u denote the uniaxial anisotropy constant (J/m^3) and Θ represent the angle between the magnetization vector $\boldsymbol{M}$ and the easy axis, Equation (10) can be explicitly formulated as [14] [15]:

$$E = -\boldsymbol{H} \cdot \boldsymbol{B} + K_u \sin^2(\Theta) \tag{11}$$

Here, letting H_{max} denote the saturation magnetic field intensity of the sensor, the total free energy expression can be detailed in terms of its explicit components as:

$$E = -\mu_0 H_{max} H_y \sin\Theta - \mu_0 H_{max} H_x \cos\Theta + \frac{1}{2}\mu_0 H_{max} H_k \sin^2(\theta) \tag{12}$$

where H_k is defined as the "anisotropy field", governed by the magnetocrystalline structure and shape anisotropy of the material according to [15]:

$$H_k = \frac{2K_u}{H_{max}} \tag{13}$$

To determine the equilibrium angle Θ in thermodynamic equilibrium, the minimum energy condition is satisfied by setting the first partial derivative of the total energy with respect to Θ to zero [15]:

$$\frac{\partial E}{\partial \Theta} = 0 \tag{14}$$

$$\frac{\partial E}{\partial \Theta} = -\mu_0 H_{max} H_y \cos\Theta + \mu_0 H_{max} H_x \sin\Theta + \mu_0 H_{max} H_k \sin(\theta)\cos(\Theta) = 0 \tag{15}$$

Performing the requisite algebraic rearrangements and simplifications on Equation (15) yields:

$$H_k \sin(\Theta)\cos(\Theta) = H_y \cos(\Theta) - H_x \sin(\Theta) \tag{16}$$

It is well-established that in low-field magnetic sensing, the angle Θ between the easy axis and the magnetization vector $\boldsymbol{M}$ assumes very small values. Applying the small-angle approximations ($\cos\Theta \approx 1$ and $\sin\Theta \approx \tan\Theta$) under these conditions gives:

$$\sin\Theta = \frac{H_y}{H_k + H_x} \tag{17}$$

Comparing the derived Equation (17) with Equation (8) established earlier demonstrates that the saturation magnetic field value, H_{max}, can be expressed as the sum of the x-component of the applied magnetic field (H_x) and the intrinsic anisotropy field of the material (H_k), such that $H_{max} = H_k + H_x$ [15]-[20]. This fundamental relation proves that applying an auxiliary bias field along the x-axis dynamically adjusts both the saturation threshold and, consequently, the overall sensitivity of the sensor.

3. Structure, Architecture, and Characteristics of the KMZ51 Sensor

3.1. Barber-Pole Geometry and Linearization

The resistance-magnetic field (R-H) characteristic of a conventional AMR sensor exhibits a parabolic, bidirectional profile, as formulated in Equation (9) (**Figure 2**). Let H_0 denote the initial magnetic field applied to the permalloy material during deposition; as the externally applied magnetic field H_y approaches zero, the ratio H_y/H_0 similarly approaches zero. Within this region, the slope of the curve vanishes, resulting in exceptionally low sensitivity. Furthermore, due to parabolic symmetry, the resistance yields the same value for two distinct magnetic field intensities even if the direction (sign) of the H_y field reverses, thereby rendering orientation determination impossible [17] [21]-[23]. To transcend this limitation and attain a linear output characteristic, a structural configuration termed the "Barber-Pole" is utilized, wherein highly conductive aluminum or gold strips are periodically deposited onto the permalloy film at an angle of 45˚ relative to the easy axis [24] [25].

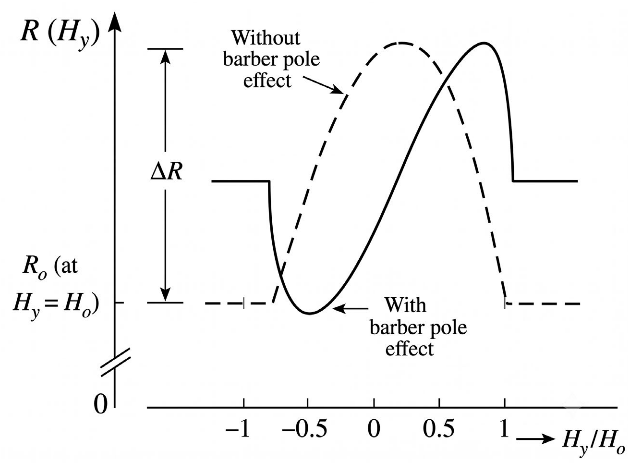

Figure 2. Resistance vs. magnetic field (R-H) characteristic curve [26].

Because the electrical conductivity of aluminum is substantially higher than that of permalloy (exhibiting an electrical resistivity approximately one-tenth that of permalloy), the current preferentially travels along the aluminum strips for the longer path, while traversing the permalloy film via the shortest path, specifically, the route perpendicular to the metallic strips. Consequently, the current flow is geometrically forced to deviate by an angle of 45˚ [23]-[25]. The angle between the current density vector and the resultant magnetization vector ($\boldsymbol{M}$), previously denoted as Θ, now shifts to either (Θ - 45˚) or (Θ + 45˚). Under these conditions, the sensor's transfer characteristic becomes asymmetric, the inflection point of the parabola shifts directly to the zero-field point, and the linear operating range is symmetrized around low H_y values, enabling both the magnitude and polarity of the magnetic field to be resolved with high precision [24].

The resistance equation governing an AMR sensor fabricated with the Barber-Pole configuration can now be formulated as [15] [24]:

$$R\left(H_y\right) = R_0 + \frac{\Delta R}{2} \pm \Delta R \frac{H_y}{H_{\max}} \sqrt{1 - \left(\frac{H_y}{H_{\max}}\right)^2} \tag{18}$$

When the square root term, $\sqrt{1 - \left(\frac{H_y}{H_{\max}}\right)^2}$, approaches unity in weak magnetic fields, the equation becomes completely linear $\left[R\left(H_y\right) \approx R_0 + \left(\Delta R/2\right) \pm \left(\Delta R/2\right)\left(H_y/H_{\max}\right)\right]$. The ± sign in the equation determines the increasing or decreasing trend of resistance with respect to the magnetic field, depending on whether the aluminum strips are placed at +45˚ or −45˚ on the permalloy [23].

3.2. Wheatstone Bridge Configuration

The KMZ51 is constructed by interconnecting four Barber-Pole configured permalloy films into a full Wheatstone bridge topology to suppress common-mode noise sources, such as temperature fluctuations and supply voltage variations, and to double the output signal amplitude [9] (**Figure 3**). Two diagonally opposite elements in the bridge possess a +45˚ Barber-Pole geometry (R_A), whereas the remaining two diagonal elements exhibit a −45˚ Barber-Pole geometry (R_B).

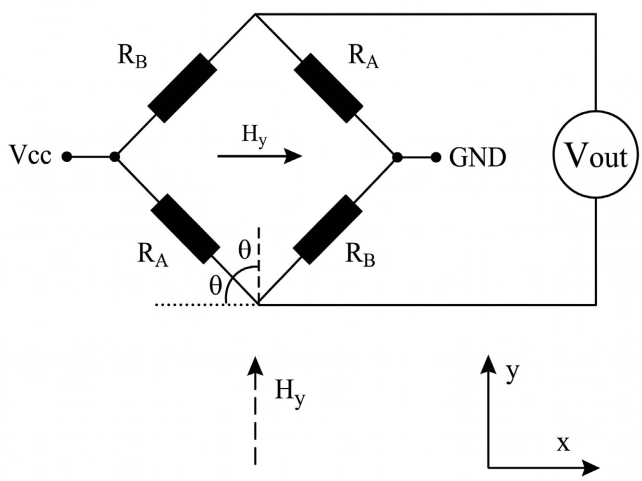

Figure 3. Equivalent Wheatstone bridge circuit.

In the equivalent circuit of the Wheatstone bridge, the differential output voltage is expressed by the general formulation [15]:

$$V_{\text{çıkış}} = V_{\text{cc}} \left(\frac{R_B - R_A}{R_A + R_B} \right) \tag{19}$$

Here, the quantities denoted by R_A and R_B represent the active resistance values of the permalloy films under the influence of the external magnetic field H_y. Utilizing Equation (18) in conjunction with the previously derived relation $H_{\max} = H_k + H_x$, these resistances can be formulated as:

$$R_A\left(H_y\right) = R_0 + \frac{\Delta R}{2} - \Delta R \frac{H_y}{H_k + H_x} \sqrt{1 - \left(\frac{H_y}{H_k + H_x} \right)^2} \tag{20}$$

$$R_B\left(H_y\right) = R_0 + \frac{\Delta R}{2} + \Delta R \frac{H_y}{H_k + H_x} \sqrt{1 - \left(\frac{H_y}{H_k + H_x} \right)^2} \tag{21}$$

Substituting Equation (20) and Equation (21) into Equation (19) eliminates the baseline resistance term R_0, yielding the exact mathematical expression for the differential output voltage [15] [23]:

$$V_{\text{out}} = V_{\text{cc}} \frac{2\Delta R}{2R_0 + \Delta R} \frac{H_y}{H_k + H_x} \sqrt{1 - \left(\frac{H_y}{H_k + H_x} \right)^2} \tag{22}$$

According to this derivation, the primary variables governing the bridge output voltage encompass the external magnetic field (H_y), the bridge supply voltage (V_{cc}), the relative magnetoresistance ratio of the material [$\Delta R/(2R_0 + \Delta R)$], and the anisotropy field intensity (H_k) established during the deposition of the film along the easy axis [15] [23].

3.3. KMZ51 Pin Configuration and Technical Parameters

The KMZ51 sensors manufactured by Philips incorporate an internal compensation coil and a flipping coil (**Figure 4**). The KMZ51 exhibits exceptional characteristics, including high sensitivity, low offset voltage, non-contact sensing capability, a broad operating frequency range (0 Hz to 1 MHz), an elevated operating

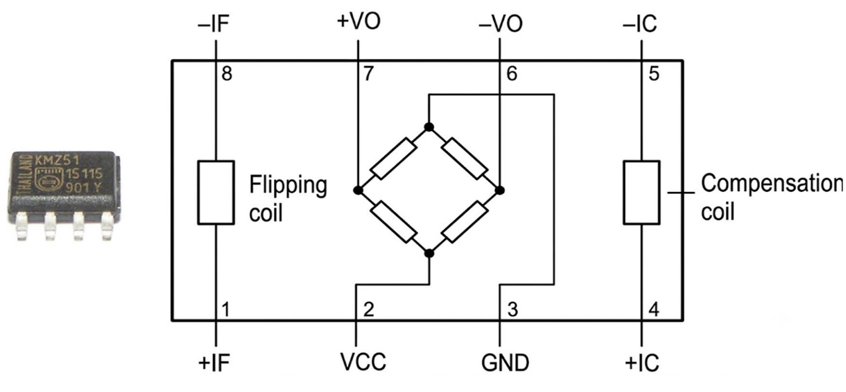

Figure 4. KMZ51 internal structure and package outline.

temperature (up to 125˚C), and an extended operational lifespan owing to its monolithic solid-state architecture [9] [10]. Enclosed within an 8-pin SO8 surface-mount package, the detailed pin configuration and electrical specifications of the sensor are presented in **Table 1** and **Table 2**, respectively [9] [10].

Table 1. KMZ51 pin configuration and functional descriptions [9].

Pin No	Symbol	Functional Description
1	$+I_{flip}$	Flipping coil positive supply terminal
2	V_{cc}	Wheatstone bridge supply voltage terminal (+5 V typical)
3	GND	Ground connection (0 V reference terminal)
4	$+I_{comp}$	Compensation coil positive supply terminal
5	$-I_{comp}$	Compensation coil negative supply terminal
6	$-V_o$	Wheatstone bridge negative differential output voltage
7	$+V_o$	Wheatstone bridge positive differential output voltage
8	$-I_{flip}$	Flipping coil negative supply terminal

Through pins 1 and 8, the internal flipping coil is driven, while pins 4 and 5 energize the compensation coil; simultaneously, the differential output voltages proportional to the external magnetic field are acquired across pins 6 and 7 [9].

Table 2. Fundamental electrical and magnetic specifications of the KMZ51 (T_{amb} = 25˚C) [9].

Symbol	Parameter Description	Minimum	Typical	Maximum	Unit
V_{cc}	Bridge supply voltage	-	5	8	V
S	Sensitivity (uncompensated bridge)	12	16	-	mV/V /(kA/m)
V_{offset}	Zero-field offset voltage	−1.5	-	+1.5	mV/V
R_{bridge}	Wheatstone bridge baseline resistance	1.0	-	3.0	kΩ
R_{comp}	Compensation coil internal resistance	100	170	300	Ω
A_{comp}	Compensation coil field factor	19	22	25	(A/m) /mA
R_{flip}	Flipping coil internal resistance	1.0	2.0	3.0	Ω
$I_{flip(min)}$	Recommended minimum flipping pulse current	800	1000	1200	mA
$t_{flip(min)}$	Minimum flipping pulse duration	1	3	100	µs

As detailed in **Table 2**, the KMZ51, which accommodates bridge supply voltages up to 8 V, features a bridge baseline resistance ranging between 1 kΩ and 3 kΩ, while achieving a typical sensitivity level of 16 (mV/V)/(kA/m) [9] [10].

3.4. Physics of the Compensation and Flipping Coils

During precision measurements executed with the sensor, the output voltage can be adversely affected by ambient temperature fluctuations or external interfering fields, potentially driving the operating point into the non-linear region and rendering accurate quantification unfeasible. The integrated compensation coil deposited directly onto the sensor generates an artificial magnetic field oriented in opposition to the external field, with a magnitude governed by the formulation [9] [15]:

$$H_{comp} = A_{comp} \times I_{comp} \tag{23}$$

When the magnitude of the resulting compensation field (H_{comp}) is adjusted to be equal in intensity and opposite in direction to the detected external magnetic field (H_{ext}), the net magnetic field acting across the sensor is nullified ($H_{net} = H_{ext} - H_{comp} = 0$). This operational mode is designated as "null-field operation" (or closed-loop feedback). The predominant physical advantage of this methodology is that it continuously constrains the sensor at the optimal linear and sensitive center point of its transfer curve, thereby substantially suppressing sensitivity drifts induced by the temperature coefficient of the permalloy material. However, residual errors such as coil-driver inaccuracies and environmental magnetic interference may still persist [10] [26].

Furthermore, if the permalloy thin film is arbitrarily exposed to an intense external magnetic field, its internal single-domain structure is disrupted, causing the magnetic domains to forfeit their easy-axis alignment and transition into a randomized multi-domain state. This degradation induces hysteresis errors and permanently shifts the zero-field output voltage (offset) of the Wheatstone bridge. To rectify this anomaly and realign the domains along the easy axis, the integrated flipping coil is utilized. Applying a brief, high-amplitude current pulse (typically t_{flip} = 3 μs, ranging between 800 mA and 1200 mA) through the flipping coil induces an intense magnetic field (approximately 3 kA/m) parallel to the easy axis across the film, thereby re-magnetizing the permalloy into a stable, single-domain state [8] [27].

The flipping mechanism not only corrects domain disturbances but also facilitates advanced signal modulation techniques. By periodically alternating the polarity of the current pulse between positive ($+I_{flip}$) and negative ($-I_{flip}$), the easy-axis magnetization of the sensor is cyclically reversed by 180˚. This inversion reverses the slope of the transfer characteristic (the algebraic sign of the sensitivity) while leaving the intrinsic offset voltage of the Wheatstone bridge unaltered. By subtracting the output signals acquired during two sequential, oppositely flipped states, calculated as $[(V_o(+) - V_o(-))/2]$, static offset voltages, thermal electromotive force (EMF) disturbances, and low-frequency 1/f (flicker) noise are significantly minimized, though base-level amplifier noise remains [8] [26] [27].

4. Performance and Error Source Analysis (Error Budget & Drift Analysis)

4.1. Temperature Drift and Its Mathematical Model

The primary environmental factor bounding the operational measurement accuracy of AMR sensors in field applications is ambient temperature fluctuation. Thermal variations directly influence both the baseline bridge resistance (R_{bridge}) and the magnetoresistive sensitivity (S) of the permalloy thin film [26] [28]. For the KMZ51 sensor specifically, the temperature coefficient of resistance (TCR) exhibits a typical magnitude of approximately +0.3%/K according to its technical specifications:

$$R_{\text{bridge}}(T) = R_{\text{bridge}}(T_0) \times \left[1 + \text{TCR} \times (T - T_0)\right] \tag{24}$$

Here, T_0 designates the reference temperature (25˚C), whereas T represents the operating ambient temperature. Conversely, the temperature coefficient of sensitivity (TCS) of the sensor demonstrates a negative trajectory, varying between −0.25%/K and −0.3%/K [9] [28]:

$$S(T) = S(T_0) \times \left[1 + \text{TCS} \times (T - T_0)\right] \tag{25}$$

If the sensor is excited by a constant voltage supply (V_{cc}), the differential output voltage attenuates at the rate of TCS as the temperature escalates. However, if the sensor is driven by a constant current source (I_{bridge}) rather than a constant voltage, the effective voltage across the bridge increases at the rate of TCR, in accordance with the relation $V_{\text{bridge}}(T) = I_{\text{bridge}} \times R_{\text{bridge}}(T)$. Because the magnitudes of TCR and |TCS| are nearly identical in the permalloy alloy, constant-current excitation provides a passive hardware-level thermal compensation, thereby suppressing the overall temperature drift by an order of magnitude [28] [29].

4.2. Cross-Axis Sensitivity

An ideal uniaxial magnetic sensor is expected to respond exclusively to the magnetic field component directed along its primary sensing axis (the y-axis, H_y). In practical KMZ51 sensors, however, geometric alignment tolerances of the permalloy thin films and distortion of the anisotropy field cause the transfer characteristic to be degraded by external fields applied along the easy axis (the x-axis, H_x) or orthogonal to the film plane (the z-axis, H_z) [15] [30]. Cross-axis sensitivity (S_{cross}) stems primarily from variations in the effective anisotropy field ($H_k + H_x$) in the denominator of the governing transfer formulation in the presence of an H_x component [Equation (22)]. A strong positive H_x field reinforces the easy axis, thereby stabilizing the sensor at the expense of attenuated sensitivity; conversely, a negative H_x field opposes the easy axis, augmenting sensitivity while inducing domain instability and severe linearity degradation. To suppress these geometric errors in multi-axis instrumentation, rigorous orthogonal sensor alignment or algorithmic ellipsoid-fitting calibration matrices are implemented [29] [31].

4.3. Hysteresis and Remanence Errors

In accordance with the fundamental nature of ferromagnetic materials, permalloy thin films exhibit a bidirectional hysteresis loop during the cyclic application and removal of an external magnetic field. Should the sensor be exposed to a transient magnetic overload exceeding its linear operating range ($H_{\max}$), such as exposure to a proximate permanent magnet or a high-current conductor, domain walls within the film undergo irreversible displacement, resulting in remanent magnetization (M_r) [8] [12]. While this hysteresis is a generic limitation of all permalloy-based AMR sensors, the KMZ51 specifically mitigates this error through its internal flipping coil architecture. Applying periodic flipping pulses forcibly resets the KMZ51's domain walls back to their stable easy-axis alignment [8] [27].

5. Comparative Performance Matrix of GMR, TMR, and Fluxgate Sensors

Magnetic field sensing technologies have undergone substantial evolution over the past three decades. Spanning a broad spectrum that encompasses conventional Hall-effect sensors, Anisotropic Magnetoresistance (AMR), Giant Magnetoresistance (GMR), Tunnel Magnetoresistance (TMR), and electromechanical/magnetic-core Fluxgate sensors, each technology exhibits distinct physical advantages and operational limitations [1] [32]. Presently, while TMR sensors deliver the highest voltage output and lowest noise floor owing to massive magnetoresistance ratios (MR%) exceeding 200% [33] [34], conventional AMR sensors such as the KMZ51 retain their industry-standard status due to mature manufacturing technologies, superior linearity, minimal hysteresis, and cost-effective monolithic architectures [6] [35].

A comprehensive quantitative and functional performance evaluation comparing the KMZ51 AMR sensor against primary competing technologies (GMR, TMR, and Fluxgate) is presented in **Table 3** [1] [6] [32] [35]-[37].

Table 3. Comparative performance matrix of the KMZ51 AMR sensor against GMR, TMR, and Fluxgate technologies.

Performance Metric	KMZ51 (AMR)	GMR Sensors	TMR Sensors	Fluxgate Sensors
MR Ratio ($\Delta R/R_0$%)	%2 - %3	%10 - %20	%100 - %300	Not Applicable (Induction)
Magnetic Field Resolution	1 nT - 10 nT	0.1 nT - 1 nT	1 pT - 100 pT	0.01 nT - 0.1 nT
Linear Operating Range	±0.1 mT to ±0.5 mT	±1 mT to ±5 mT	±0.05 mT to ±1 mT	±0.1 mT to ±0.2 mT
Typical Power Consumption	Low (<15 mW)	Low (<15 mW)	Ultralow (<1 mW)	High (100 - 500 mW)
1/f Noise Level	Low (Ultralow via flipping)	Moderate to High	High (Thin tunnel barrier)	Ultralow
Temperature Stability (−40/+125˚C)	High (Coil-compensated)	Moderate	Moderate to Low (Tunnel drift)	High
Manufacturing Cost and Integration	Low (Mature thin-film IC)	Moderate (Multilayer IC)	High (Complex nanolithography)	Very High (Coil/core winding)

An analysis of **Table 3** reveals that although Fluxgate sensors provide superior magnetic resolution, their elevated power consumption, bulky and heavy physical form factors, and prohibitive manufacturing costs preclude their implementation in micro-scale integrated systems [4]. Conversely, despite generating substantially higher absolute output signals, GMR and TMR sensors necessitate rigorous calibration protocols due to prominent 1/f noise characteristics, inherent hysteresis tendencies, and nanofabrication complexities [33] [34]. Consequently, through its integrated Barber-Pole linearization and internal compensation/flipping coil architecture, the KMZ51 delivers the optimal signal stability-to-cost ratio for applications operating within the magnitude of the Earth's magnetic field (25 - 65 μT) [6] [37].

6. Signal Processing and Noise Mitigation Circuit Architectures

6.1. Synchronous Detection (Lock-In Detection/Chopping) Topology

The millivolt-level output signals of the KMZ51 sensor can be severely degraded or completely obscured by the 1/f noise and thermal drift of operational amplifiers, particularly within the direct current (DC) or very low-frequency regime (<10 Hz). To overcome this limitation, a synchronous modulation and demodulation (lock-in detection) topology is implemented specifically utilizing the KMZ51's integrated flipping coil, as experimentally validated by Hauser *et al.* [8]. A square wave alternating at a modulation frequency f_{mod} between 1 kHz and 30 kHz is generated by a microcontroller or a dedicated oscillator circuit. This excitation signal is applied to the flipping coil ($+I_{flip}/-I_{flip}$) as current pulses via an H-bridge driver stage [27] [30].

During this modulation cycle, because the easy-axis magnetization of the sensor is cyclically inverted by 180˚ at the frequency f_{mod}, the magnetic field-dependent differential output signal of the bridge is transposed into an alternating current (AC) signal centered at the f_{mod} carrier frequency. Conversely, the static offset voltage of the bridge, thermal electromotive force (EMF) anomalies, and the intrinsic $1/f$ noise of the amplifier remain confined to the DC (0 Hz) baseband [8] [38]. The modulated differential signal is subsequently amplified by an instrumentation amplifier (e.g., INA114 or AD620) featuring a high common-mode rejection ratio (CMRR > 100 dB). The amplified AC signal is then down-converted back to DC by an analog switch (acting as a synchronous demodulator or lock-in amplifier) phase-locked to the f_{mod} reference frequency, after which it is routed through a low-pass filter (LPF). This topology effectively reduces the sensor's noise floor to nanotesla levels and substantially mitigates zero-field offset drift, with calibration error and residual electronic noise remaining as the primary constraints [30] [38].

6.2. Closed-Loop Current Feedback Architecture

For high-precision laboratory instrumentation, electronic compasses, and aerospace systems, optimal measurement accuracy is achieved by operating the KMZ51 sensor in a closed-loop current feedback mode [10] [26]. Within this architectural paradigm, the differential output signal of the Wheatstone bridge is directed through an integrator (or a proportional-integral, PI, controller) stage to a voltage-to-current (V/I) converter. The output of the V/I converter is connected directly across pins 4 and 5 of the sensor, driving the integrated compensation coil (I_{comp}) [9] [26].

When the system is subjected to an external magnetic field (H_{ext}), an instantaneous error voltage is generated across the bridge terminals. The PI controller immediately registers this error and drives an automated compensation current, I_{comp}, through the internal coil to generate a magnetic field ($H_{comp} = -H_{ext}$) that precisely opposes the ambient field [Equation (23)]. Consequently, the differential output voltage of the sensor bridge is continuously locked at zero volts ($V_{out} = 0$ V) [26]. Under this operational scheme, the measurement datum is no longer derived from the bridge voltage; instead, it is acquired by precisely quantifying the compensation current I_{comp} traversing the coil (or by measuring the potential drop across a high-precision shunt resistor). This closed-loop architecture suppresses non-linearity errors below 0.01% and largely mitigates the temperature coefficient of sensitivity (TCS), expanding the dynamic operating range of the sensor [10] [26] [29].

7. KMZ51-Based Advanced Technological Applications

7.1. Electronic Compasses and Navigation Systems

One of the most classical and widespread applications of the KMZ51 is its deployment in electronic compasses and orientation tracking systems, as demonstrated by Morgan [26] and Fang *et al.* [29]. The Earth's magnetic field exhibits a relatively low intensity, ranging approximately between 25 μT and 65 μT depending on geographic location [28] [39]. To resolve magnetic vectors at these magnitudes with an angular precision of 0.1˚ to 0.5˚, low-noise and highly linear KMZ51 sensors (alongside their dual-axis counterpart, the KMZ52) are widely deployed [28] [40].

In practical navigation architecture, two orthogonal KMZ51 sensors are aligned along the X- and Y-axes to quantify the horizontal components of the geomagnetic field. However, when the compass module is tilted relative to the horizontal plane, the robust vertical component (Z-axis) of the Earth's magnetic field projects onto the horizontal sensing axes, inducing significant heading errors [29] [39]. Consequently, modern electronic compass designs integrate 3-axis MEMS accelerometers alongside 3-axis magnetic measurement systems to execute real-time tilt compensation [29] [40]. Furthermore, static magnetic deviations originating from permanent ferromagnetic structures within the host vehicle, vessel, or aircraft (hard-iron effects), as well as ellipsoidal distortions caused by induced magnetization in surrounding structural metals (soft-iron effects), are systematically mitigated using ellipsoid-fitting algorithms and automated instrumentation calibration matrices [29] [31]. A dominant limitation in electronic compass applications is the susceptibility to tilt errors and local magnetic interference (hard and soft-iron effects), which necessitate continuous dynamic calibration to prevent significant heading degradation.

7.2. Intelligent Transportation and Traffic/Vehicle Detection Systems

Within intelligent transportation systems (ITS), monitoring traffic density, conducting vehicle counts, performing speed estimation, and managing signalized intersections rely heavily on detecting instantaneous anomalies (magnetic anomalies) induced in the Earth's magnetic field by passing ferromagnetic vehicle bodies [25]. In a pioneering study conducted by Kang *et al.* (2005), a KMZ51-based vehicle detector was engineered and experimentally validated under rigorous highway conditions [25]. The authors demonstrated that the Wheatstone bridge architecture of the sensor successfully resolves and discriminates the characteristic magnetic signatures originating from vehicle engine blocks, chassis structures, and wheel axles with high accuracy [25].

Compared to conventional inductive loop detectors, KMZ51-based AMR sensor networks represent an indispensable traffic monitoring infrastructure for smart cities due to distinct deployment advantages: they can be seamlessly retrofitted into road surfaces via minimal core drilling, remain impervious to pavement degradation and rutting, feature low power consumption (<15 mW) enabling multi-year autonomous operation via battery or solar harvesting, and exhibit zero performance degradation under adverse meteorological conditions such as snow, precipitation, and dense fog [25] [41].

7.3. Non-Contact and Yokeless Current Measurement Systems

Within power electronics, electric vehicle (EV) charging infrastructures, and smart grids, the galvanically isolated and non-contact measurement of elevated AC and DC currents is of paramount importance. Conventional Hall-effect current transducers typically necessitate heavy, bulky ferromagnetic toroidal cores (magnetic flux concentrators) to concentrate on the magnetic field generated by the current-carrying conductor, inherently introducing severe magnetic hysteresis and saturation limitations [42] [43].

The high sensitivity of the KMZ51 sensor, reaching the nanotesla regime, completely eliminates the necessity for ferromagnetic flux concentrators, thereby enabling advanced "yokeless" current measurement architectures [42]. In innovative measurement systems developed by Mlejnek and Ripka (2016) as well as Ripka and Janosek (2006), a circular AMR sensor array was constructed by arranging 4 or 8 KMZ51 sensors in an axisymmetric configuration around a current-carrying busbar or conductor [25] [43]. In accordance with Ampère's Circuital Law, this circular array collectively measures the tangential magnetic field generated by the primary current while completely rejecting external homogeneous magnetic noise and stray fields from adjacent conductors through differential signal processing

[42] [43]. This architecture is capable of quantifying currents scaling up to thousands of amperes without encountering core saturation phenomena, achieving measurement error margins below 0.1%, extensive frequency bandwidths, and minimal hardware mass [42] [43]. The primary limitation of yokeless current measurement architectures is their high sensitivity to conductor-position variations and susceptibility to stray magnetic fields from adjacent conductors, requiring precise mechanical alignment.

7.4. Defense Applications, Mine Detection, and Magnetic Gradiometers

Within the defense and security sectors, the detection of weak magnetic anomalies, specifically buried unexploded ordnance (UXO) and ferromagnetic or semi-metallic landmines, is of critical importance [43]. To eliminate diurnal geomagnetic fluctuations (such as power grid interference and solar wind disturbances), instrument architectures deploy "magnetic gradiometers," which substitute a single magnetometer with a dual-sensor KMZ51 configuration arranged in parallel or differential alignment across a fixed spatial baseline (e.g., a 30 cm separation) [43].

In an experimental study conducted by Vyhnánek *et al.* (2012), an axial AMR gradiometer was fabricated using two KMZ51 sensors to develop a continuous-wave excitation mine detection platform [43]. The engineered system successfully resolved both ferromagnetic metals and diamagnetic signatures with high precision. The investigation proved that even a compact aluminum target measuring merely 50 mm × 50 mm could be detected at a soil burial depth of approximately 20 cm with a robust signal-to-noise ratio [43]. This topology has been successfully integrated into military reconnaissance robotics, border surveillance networks, and submarine anomaly detection architectures (e.g., Magnetic Anomaly Detection, MAD) [43] [44].

7.5. Small Satellite (CubeSat/NanoSat) Attitude Determination and Control Systems (ADCS)

The proliferation of microsatellites, NanoSats, and CubeSats within the aerospace industry has accelerated the demand for lightweight, low-power, and radiation-tolerant Attitude Determination and Control Systems (ADCS) [41] [44]. To maintain accurate orbital orientation, point solar arrays toward the sun, and lock communication antennas onto ground stations, satellites require continuous 3-axis vector measurements of the Earth's geomagnetic field [41] [44].

Conventional high-precision Fluxgate magnetometers deployed on large-scale satellites remain excessively heavy and power-intensive for the stringent volume ($1U = 10 \times 10 \times 10\ cm^3$) and energy budgets characteristic of CubeSat platforms [4]. Consequently, commercial AMR sensors such as the KMZ51 have emerged as primary magnetometer payloads within CubeSat ADCS architectures [41] [44]. Compared to standard semiconductor materials, the thin-film permalloy alloy exhibits intrinsic solid-state radiation tolerance against cosmic radiation and Total Ionizing Dose (TID) degradation, ensuring years of drift-free operation in space environments [41] [44]. Furthermore, integrated flipping coils enable autonomous, on-orbit zero-point calibration throughout the operational lifespan of the mission [41] [44].

7.6. Nondestructive Testing (NDT) and Magnetic Flux Leakage (MFL) Inspection Systems

Nondestructive Testing (NDT) methodologies are widely deployed to inspect industrial metallurgy, oil and gas pipelines, railway infrastructure, and structural steel frameworks [6] [45]. Among magnetic evaluation techniques, the Magnetic Flux Leakage (MFL) method represents one of the most effective diagnostic approaches [45]. Specifically, studies by Coramik *et al.* [46] and Ege *et al.* [47] have demonstrated that KMZ51 arrays provide superior signal stability in MFL evaluations compared to generic Hall-effect sensors. The ferromagnetic steel structure under examination (such as a pipeline wall) is magnetized to near-saturation levels utilizing permanent magnets or excitation windings [45].

In the absence of internal fractures, corrosion, voids, or geometric cross-sectional reductions, magnetic flux lines propagate homogeneously through the steel matrix. However, when a surface or subsurface micro-crack or localized corrosion is present, the low magnetic permeability of the resulting air gap forces the magnetic flux lines to refract outward, leaking into the surrounding ambient air [45]. KMZ51 AMR sensor arrays positioned in close proximity to the inspection surface detect the spatial gradient and distortion components of these microscopic flux leakages with high resolution [6] [45]. The compact, micrometer-scale thin-film sensing area of the transducer enables precise millimeter-scale mapping of fracture geometries and accurate depth profiling of pipeline corrosion [6] [45]. For MFL inspections, the dominant deployment constraint is the lift-off variation; minor fluctuations in the distance between the AMR sensor and the inspection surface can severely degrade the accuracy of the magnetic anomaly signature.

8. Review of Key KMZ51 Studies in the Literature

A comprehensive chronological and thematic summary of critical experimental investigations published in international peer-reviewed journals, demonstrating the theoretical superiority, signal conditioning capabilities, and field application success of the KMZ51 sensor, is presented in **Table 4** [8] [24]-[29] [36] [42] [43].

Table 4. Summary of fundamental research and performance outcomes conducted with the KMZ51 AMR sensor in the literature.

Author and Year	Research/ Application Domain	Implemented Methodology/Circuit Architecture	Key Findings and Performance Outcomes
Morgan, D. V. (2009) [26]	Electronic compass and orientation tracking	KMZ51/52 paired with an instrumentation amplifier and internal coil-reset topology.	Achieved <0.5˚ heading accuracy in the geomagnetic field; offset and thermal drift were suppressed via coil excitation pulses.

Continued

Hauser *et al.* (2003) [8] [24]	AMR sensor stability and flipping analysis	Domain-wall resetting and characterization utilizing high-current pulses (±1000 Ma, 3 μs).	Hysteresis errors were reduced below 0.1%; periodic flipping suppressed the sensor's $1/f$ noise floor by an order of magnitude.
Mlejnek *et al.* (2008) [24]	Switched capacitor flipping circuitry for KMZ51	Generation of narrow, high-current flipping pulses (up to 2.8 A) utilizing switched-capacitor arrays instead of direct continuous drive.	The capacitor-based discharge topology provided the intense magnetic saturation required to remove hysteresis while maintaining an extremely low average power dissipation (~30 mW), facilitating integrated system compatibility.
Kang *et al.* (2005) [40]	Traffic monitoring and vehicle detection systems	Single-axis KMZ51 detector embedded in pavement paired with a real-time anomaly algorithm.	Achieved >98% vehicle detection accuracy in highway trials; extracted characteristic engine and chassis magnetic signatures.
Ripka & Janosek (2010) [6].	Non-contact current measurement arrays	Axisymmetric circular array of multiple KMZ51 sensors arranged around a conductor.	Quantified high AC/DC currents without a toroidal core (yoke); external magnetic interference was canceled via differential array processing.
Fang *et al.* (2011) [29]	Magnetic compass calibration algorithms	Ellipsoid-fitting algorithms for hard-iron and soft-iron compensation in KMZ51/52 sensor networks.	Sensor calibration error was reduced by 80% in complex magnetic interference environments; successfully integrated into autonomous vehicles.
Vyhnánek *et al.* (2012) [43]	Defense applications and landmine detection	Axial AMR gradiometer constructed with two KMZ51 sensors utilizing continuous-wave excitation.	Resolved weak ferromagnetic and diamagnetic targets measuring 50 × 50 mm at a burial depth of 20 cm with a high signal-to-noise ratio.
Ozyagcilar, T. (2012) [30]	Tilt-compensated electronic compass design	Data fusion of 3-axis magnetic reading with 3-axis MEMS accelerometer measurements.	Enabled drift-free computation of true north orientation across 360-degree spatial rotation regardless of device tilt angle.
Mlejnek & Ripka (2016) [25]	High-precision yokeless current transducer	Advanced yokeless circular geometry consisting of 8 KMZ51 sensors with algorithmic compensation.	Individual manufacturing tolerances across sensor parameters were mitigated via software compensation; reached the 0.05% accuracy class.

Continued

Ripka, P. (2019) [28]	Advanced magnetic field sensors review	Contemporary performance characterization across AMR, GMR, TMR, and Fluxgate technologies.	Confirmed that the KMZ51 maintains its industry-standard status for scientific and industrial applications due to mature fabrication technology and a low noise floor.
Çıtak (2020) [48]	Pulse-induction metal detector and pipeline inspection	KMZ51 AMR sensor module interfaced with an NI USB-6210 DAQ card and LabVIEW real-time reading interface.	Post-pulse damping characteristics were precisely quantified, achieving rapid response times for defect identification.
Muşuroi *et al.* (2020) [49]	Non-contact DC/AC current measurement and sensor comparison	Circular array of 8 KMZ51 AMR sensors arranged around a conductor with set/reset resetting circuitry.	Achieved very low linearity error (0.05%) and high measurement precision across extensive current ranges.
Coramik *et al.* (2023) [46]	Nondestructive pipeline inspection (PIG) via magnetic flux leakage (MFL)	ANSYS Maxwell simulations and an experimental comparison circuit evaluating AMR vs. Hall-effect sensors.	Evaluated the influence of scanning velocity on sensor output, demonstrating superior signal stability of AMR sensors under varying operational speeds.
Ege *et al.* (2020) [47]	Detection and depth profiling of subterranean ferromagnetic structures	AMR sensor arrays mounted on a 3-axis mechanical scanning platform combined with Artificial Neural Networks (ANN).	High-accuracy mapping of surface geometry and depth localization for buried subsurface objects was achieved.
Wu *et al.* (2021) [50]	Corrosion detection under protective coatings in metallic structures	AMR sensor surface scans operating on combined principles of magnetic flux leakage and eddy currents.	Successfully detected underlying corrosion without removing protective coatings by suppressing lift-off interference effects.
Muşuroi *et al.* (2025) [51]	Non-contact measurement of weak magnetic fields and low DC/AC currents (0 - 100 mA).	Multi-bridge architecture comprising two antiphase differential AMR bridges integrated on a compact die with an overlaid U-shaped silver-printed current trace.	Stable measurements were achieved in DC and AC modes with a low detection threshold (~10 μA) and approximately 7.5% linearity error. System sensitivity was evaluated across the microtesla to millitesla regime.

As demonstrated by the chronological and thematic literature summary in **Table 4**, the KMZ51 sensor has evolved far beyond a simple sensing element; integrated with flipping coils, instrumentation amplifiers, lock-in modulators, and advanced calibration algorithms, it has left a profound imprint on the research community as a comprehensive, monolithic system architecture [6] [8] [25] [36] [42] [46]-[51].

9. Discussion and Future Trends

9.1. Contemporary Status of AMR Technology

Magnetic field sensor technologies have diversified substantially over the past three decades. Currently, while TMR sensors hold laboratory benchmarks regarding absolute sensitivity and massive magnetoresistive ratios [33] [34], AMR sensors continue to serve as the industrial workhorse across parameters of maturity, reliability, linearity, and low fabrication cost [6] [35]. Comparative analyses indicate that although AMR sensors yield lower absolute signal amplitudes relative to GMR and TMR counterparts, they provide superior signal-to-noise ratios in low-frequency operational regimes owing to minimal $1/f$ noise characteristics and negligible parasitic hysteresis [6] [37].

Evaluated within this context, although the KMZ51 sensor may appear conventional compared to modern monolithic TMR or digital-output magnetometers, it continues to provide a foundational hardware reference standard due to its superior linearity, integrated coil architecture, and documented field reliability in electronic compasses, vehicle detection networks, nondestructive evaluation platforms, and yokeless current measurement architectures [6] [52]. Furthermore, the sensor's integrated flipping and compensation coils afford external hardware designers' direct intervention into transducer physics, facilitating sophisticated noise mitigation topologies such as synchronous lock-in detection [8] [38].

9.2. IoT, Smart Cities, and MEMS Integration

The widespread adoption of Internet of Things (IoT) architectures and Smart City infrastructures has fundamentally altered functional requirements for transducer technologies. Modern sensor nodes are required not only to acquire physical data, but also to maintain continuous operation under sub-milliwatt power budgets, seamlessly interface with wireless communication protocols (e.g., LoRa, NB-IoT, Zigbee), and execute edge data processing [35] [37].

Due to their adaptability to sub-milliwatt operational envelopes and inherent solid-state robustness, AMR sensors exhibit substantial potential within IoT-based infrastructures. Although the standard KMZ51 transducer is housed within a conventional SO8 thin-film package, future trajectories point toward dense monolithic integration of AMR thin films with Micro-Electro-Mechanical Systems (MEMS) [6] [37]. This technological convergence will facilitate the fabrication of 9-degree-of-freedom (9-DoF) inertial navigation modules, combining 3-

axis AMR magnetometers, 3-axis MEMS accelerometers, and gyroscopes onto a single microscopic silicon die, thereby establishing standard hardware configurations for autonomous micro-drones, robotic joint encoders, and wearable biomedical telemetry systems [37] [53].

9.3. Artificial Intelligence and Machine Learning-Enabled Magnetic Sensing

In recent years, the integration of artificial intelligence (AI) and machine learning (ML) algorithms directly into embedded sensor nodes (Edge AI) has initiated a paradigm shift in magnetic sensing architectures [35] [37]. While conventional instrumentation processes analog data from the KMZ51 sensor using simple static thresholding or classical linear filtering, contemporary deep learning networks (such as Convolutional Neural Networks, CNN, or Long Short-Term Memory architectures, LSTM) are capable of extracting highly complex time-series patterns directly from raw transducer outputs [25] [35].

From the perspective of magnetic field instrumentation, artificial intelligence methodologies open new technological frontiers across several critical domains:

- Vehicle classification (discriminating among passenger vehicles, transit buses, heavy freight trucks, and motorcycles) and dynamic velocity estimation within traffic monitoring networks [25] [35]
- Geometric categorization of microscopic fractures and autonomous defect mapping within NDT and MFL pipeline inspection systems [45]
- Adaptive noise cancellation and calibration-free interference rejection in industrial environments characterized by severe electromagnetic interference [29] [35]
- Autonomous, real-time neural network calibration of dynamic hard-iron and soft-iron distortions in advanced electronic compass systems [29] [31]

10. Conclusions

This comprehensive review has examined the KMZ51 magnetic field sensor, one of the most successful commercial and industrial reference platforms in anisotropic magnetoresistive sensing technology, from theoretical principles to practical field implementation. Beginning with the historical evolution originating from Lord Kelvin's foundational discovery in 1856, the analysis elaborated on the quantum mechanical scattering foundations of the AMR effect, Stoner-Wohlfarth free energy formulations, and easy-axis uniaxial anisotropy modeling.

Regarding transducer architecture, the analysis detailed the Barber-Pole strip geometry, which transforms the intrinsic parabolic, symmetrical transfer characteristic of permalloy into an asymmetric, linear operational curve, alongside Wheatstone bridge differential equations and SO8 package electrical parameters [9] [10]. Primary field error sources, including temperature drift (TCR/TCS), cross-axis sensitivity, and hysteresis degradation, were mathematically modeled; subsequent evaluations demonstrated how synchronous lock-in detection and closed-loop null-field feedback architectures utilizing integrated flipping and compensation coils successfully eliminate these deviations [8] [26] [27] [38].

A comparative performance matrix evaluating the KMZ51 against GMR, TMR, and Fluxgate technologies (**Table 3**) provided quantitative verification as to why the sensor retains its industry-standard status for measurements within the magnitude of the Earth's geomagnetic field (the nanotesla to microtesla regime) fulfilling the core criteria of cost-effectiveness, highly linear output, robust internal coil integration, and documented solid-state reliability [1] [6] [32] [35]. Furthermore, an extensive literature review of experimental studies (**Table 4**) across intelligent transportation networks, electronic compasses, yokeless current arrays, defense gradiometers, CubeSat orientation systems, and nondestructive pipeline inspection confirmed the sensor's broad interdisciplinary adaptability [25] [36] [41]-[43] [45].

Consequently, despite competing with contemporary TMR and digital sensing platforms, the KMZ51 remains a cornerstone of magnetic field sensing due to its mature thin-film fabrication technology and hardware-level flexibility [6] [54]-[56]. Moving forward, AMR technology hybridized with MEMS integration, wireless IoT networks, and AI-driven noise filtering algorithms will continue to serve as an inspiring reference platform for next-generation autonomous sensing systems [37] [53] [56].

In addition to these domains, KMZ51 AMR sensors extend beyond conventional electrical engineering and industrial automation; they play a critical role in architectural engineering by ensuring structural safety, guiding advanced construction material selection, and executing nondestructive evaluation (NDT) [57]. In particular, within the Self-Magnetic Flux Leakage (SMFL) methodology, developed to monitor the elasto-magnetic behavior of ferromagnetic reinforcement steel and structural members under mechanical stress, the natural remanent magnetization variations of materials are evaluated under the Earth's ambient geomagnetic field [57] [58]. Conventional, bulky fluxgate magnetometers frequently encounter physical and operational limitations during subsurface micro-anomaly scanning in reinforced concrete due to large probe dimensions and high-power consumption. Conversely, the KMZ51 sensor, utilizing its millimeter-scale thin-film structure, linear output characteristic, and high sensitivity, enables precise spatial mapping of internal corrosion, fatigue micro-fractures, and localized stress concentrations within construction materials [58]. Consequently, the KMZ51 will persist as an inspiring, reliable, and industrial reference transducer platform for optimal material selection in modern architecture, autonomous in-situ Structural Health Monitoring (SHM), and comparative material degradation analysis in heritage building restoration.

Author Contributions

All authors contributed equally to the conceptualization, literature review, writing, and critical revision of this manuscript. All authors have read and approved the final version.

Conflicts of Interest

The authors declare no conflicts of interest regarding the publication of this paper.

References

[1] Ripka, P. (2021) Magnetic Sensors and Magnetometers. Artech House.

[2] Tumanski, S. (2001) Thin Film Magnetoresistive Sensors. IOP Publishing Ltd. https://doi.org/10.1887/0750307021

[3] Lenz, J.E. (1990) A Review of Magnetic Sensors. *Proceedings of the IEEE*, **78**, 973-989. https://doi.org/10.1109/5.56910

[4] Nazlibilek, S., Ege, Y., Kalender, O., Sensoy, M.G., Karacor, D. and Sazlı, M.H. (2012) Identification of Materials with Magnetic Characteristics by Neural Networks. *Measurement*, **45**, 734-744. https://doi.org/10.1016/j.measurement.2011.12.017

[5] Lenz, J. and Edelstein, S. (2006) Magnetic Sensors and Their Applications. *IEEE Sensors Journal*, **6**, 631-649. https://doi.org/10.1109/jsen.2006.874493

[6] Ripka, P. and Janosek, M. (2010) Advances in Magnetic Field Sensors. *IEEE Sensors Journal*, **10**, 1108-1116. https://doi.org/10.1109/jsen.2010.2043429

[7] McGuire, T. and Potter, R. (1975) Anisotropic Magnetoresistance in Ferromagnetic 3D Alloys. *IEEE Transactions on Magnetics*, **11**, 1018-1038. https://doi.org/10.1109/tmag.1975.1058782

[8] Hauser, H., Fulmek, P.L., Haumer, P., Vopalensky, M. and Ripka, P. (2003) Flipping Field and Stability in Anisotropic Magnetoresistive Sensors. *Sensors and Actuators A*: *Physical*, **106**, 121-125. https://doi.org/10.1016/s0924-4247(03)00148-1

[9] Philips Semiconductors (1998) KMZ51 Magnetic Field Sensor Datasheet. https://www.alldatasheet.com/datasheet-pdf/view/17844/PHILIPS/KMZ51.html

[10] Philips Semiconductors (1998) Magnetic Field Sensor. Philips Semiconductors, SC17, 20. https://www.mikrocontroller.net/attachment/73039/SC17_GENERAL_MAG_98_1.pdf

[11] Thomson, W. (1857) XIX. On the Electro-Dynamic Qualities of Metals: Effects of Magnetization on the Electric Conductivity of Nickel and of Iron. *Proceedings of the Royal Society of London*, **8**, 546-550. https://doi.org/10.1098/rspl.1856.0144

[12] Freitas, P.P., Ferreira, R., Cardoso, S. and Cardoso, F. (2007) Magnetoresistive Sensors. *Journal of Physics*: *Condensed Matter*, **19**, Article ID: 165221. https://doi.org/10.1088/0953-8984/19/16/165221

[13] Ritzinger, P. and Výborný, K. (2023) Anisotropic Magnetoresistance: Materials, Models and Applications. *Royal Society Open Science*, **10**, Article ID: 230564. https://doi.org/10.1098/rsos.230564

[14] Tumanski, S. (2016) Handbook of Magnetic Measurements. CRC Press.

[15] Ranchal, R., Torija, M., López, E., Sánchez, M.C., Aroca, C. and Sánchez, P. (2002) The Influence of Anisotropy on the Magnetoresistance of Permalloy-Copper-Permalloy Thin Films. *Nanotechnology*, **13**, 392-397. https://doi.org/10.1088/0957-4484/13/3/330

[16] Tumanski, S. (2013) Modern Magnetic Field Sensors: A Review. *Organ Stowarzyszenia Elektryków Polskich*, *10*, 1-12. http://www.tumanski.x.pl/01_PE_10_13_1-12_tumanski.pdf

[17] Jogschies, L., Klaas, D., Kruppe, R., Rittinger, J., Taptimthong, P., Wienecke, A., *et al.* (2015) Recent Developments of Magnetoresistive Sensors for Industrial Applications.

Sensors, **15**, 28665-28689. https://doi.org/10.3390/s151128665

[18] Yang, S. and Zhang, J. (2021) Current Progress of Magnetoresistance Sensors. *Chemosensors*, **9**, Article 211. https://doi.org/10.3390/chemosensors9080211

[19] Grosz, A., Haji-Sheikh, M.J. and Mukhopadhyay, S.C. (2017) High Sensitivity Magnetometers. Springer. https://link.springer.com/book/10.1007/978-3-319-34070-8

[20] Binasch, G., Grünberg, P., Saurenbach, F. and Zinn, W. (1989) Enhanced Magnetoresistance in Layered Magnetic Structures with Antiferromagnetic Interlayer Exchange. *Physical Review B*, **39**, 4828-4830. https://doi.org/10.1103/physrevb.39.4828

[21] Kuijk, K., van Gestel, W. and Gorter, F. (1975) The Barber Pole, a Linear Magnetoresistive Head. *IEEE Transactions on Magnetics*, **11**, 1215-1217. https://doi.org/10.1109/tmag.1975.1058886

[22] Sensitec GmbH (2024) AFF755B Magnetoresistive Field Sensor. https://www.sensitec.com/wp-content/uploads/2024/07/SENSITEC_AFF755B-DSE07.pdf

[23] Murata Manufacturing (2018) Basic Knowledge of AMR Sensors (Technical Note). https://www.murata.com/products/sensor/amr/overview/basic

[24] Mlejnek, P., Vopálenský, M. and Ripka, P. (2008) AMR Current Measurement Device. *Sensors and Actuators A*: *Physical*, **141**, 649-653. https://doi.org/10.1016/j.sna.2007.10.016

[25] Mlejnek, P. and Ripka, P. (2016) AMR Yokeless Current Sensor with Improved Accuracy. *Procedia Engineering*, **168**, 900-903. https://doi.org/10.1016/j.proeng.2016.11.301

[26] Morgan, D.V. (2009) Electronic Compass Design Using KMZ51 and KMZ52 Sensors (Philips Application Note). Philips Semiconductors. https://d1.amobbs.com/bbs_upload782111/files_29/ourdev_554701.pdf

[27] Rousseau, O., Flament, S., Guillet, B., Sing, M.L.C. and Méchin, L. (2017) Magnetic Sensors Based on AMR Effect in LSMO Thin Films. *Proceedings*, 1, Article 635. https://doi.org/10.3390/proceedings1040635

[28] Ripka, P. (2019) Contactless Measurement of Electric Current Using Magnetic Sensors. *Technisches Messen*, **86**, 586-598. https://doi.org/10.1515/teme-2019-0032

[29] Fang, J. C., Sun, H. W., Cao, J. J., Zhang, X., & Tao, Y. (2011) A Novel Calibration Method of Magnetic Compass Based on Ellipsoid Fitting. *IEEE Transactions on Instrumentation and Measurement*, **60**, 2053-2061. https://doi.org/10.1109/tim.2011.2115330

[30] Ozyagcilar, T. (2012) Calibrating an eCompass in the Presence of Hard- and Soft-Iron Interference (Freescale Semiconductor Application Note AN4246). Free-Scale Semiconductor. https://www.nxp.com/docs/en/application-note/AN4246.pdf

[31] Cai, Y., Zhao, Y., Ding, X. and Fennelly, J. (2012) Magnetometer Basics for Mobile Phone Applications. https://www.nicap.org/madar/smart_phones/Magnetometer_Basics_For_Mobile_Phone_Applications-2012.pdf

[32] Daughton, J.M. (1992) Magnetoresistive Memory Technology. *Thin Solid Films*, **216**, 162-168. https://doi.org/10.1016/0040-6090(92)90888-i

[33] Wang, S.X. and Li, G.X. (2008) Advances in Giant Magnetoresistance Biosensors with Magnetic Nanoparticle Tags: Review and Outlook. *IEEE Transactions on Magnetics*, **44**, 1687-1702. https://doi.org/10.1109/tmag.2008.920962

[34] Ma, Y., Guo, X., Li, J., Wang, W., Chen, Y., Pan, J., *et al.* (2026) A Survey on Magnetic Sensing and Communication: Technologies, Sensors, and Applications. *IEEE Communications Surveys & Tutorials*, **28**, 1776-1802.

https://doi.org/10.1109/comst.2025.3578396

[35] Lin, S., Lai, M. and Fang, W. (2024) On the Influence of Magnetic Flux Guide Location to the Out-of-Plane Magnetic Field Sensing of Chip-Scale AMR Sensor. *Sensors and Actuators A*: *Physical*, **375**, Article ID: 115517. https://doi.org/10.1016/j.sna.2024.115517

[36] Wang, S. and Gao, J. (2023) Overview of Magnetic Field Sensor. *Journal of Physics*: *Conference Series*, **2613**, Article ID: 012012. https://doi.org/10.1088/1742-6596/2613/1/012012

[37] Reininger, T. and Hanisch, C. (1997) Magnetic Field Sensors for the Industrial Automation. *Sensors and Actuators A*: *Physical*, **59**, 177-182. https://doi.org/10.1016/s0924-4247(97)80170-7

[38] Ripka, P. (1996) Noise and Stability of Magnetic Sensors. *Journal of Magnetism and Magnetic Materials*, **157**, 424-427. https://doi.org/10.1016/0304-8853(95)01177-3

[39] Caruso, M.J. (1997) Applications of Magnetoresistive Sensors in Navigation Systems. SAE Technical Paper 970602. https://doi.org/10.4271/970602

[40] Kang, M.H., Choi, B.W., Koh, K.C., Lee, J.H. and Park, G.T. (2005) Experimental Study of a Vehicle Detector with an AMR Sensor. *Sensors and Actuators A*: *Physical*, **118**, 278-284. https://doi.org/10.1016/j.sna.2004.09.002

[41] Li, W. and Wang, J. (2014) Magnetic Sensors for Navigation Applications: An Overview. *Journal of Navigation*, **67**, 263-275. https://doi.org/10.1017/s0373463313000544

[42] Ziegler, S., Woodward, R.C., Iu, H.H. and Borle, L.J. (2009) Current Sensing Techniques: A Review. *IEEE Sensors Journal*, **9**, 354-376. https://doi.org/10.1109/jsen.2009.2013914

[43] Vyhnánek, J., Janošek, M. and Ripka, P. (2012) AMR Gradiometer for Mine Detection. *Sensors and Actuators A*: *Physical*, **186**, 100-104. https://doi.org/10.1016/j.sna.2012.03.007

[44] Spier, S. (2023) Calibration of Sensors for Attitude Determination on CubeSats for Optical Inter-Satellite Links. Ph.D. Thesis, Technische Hochschule Mittelhessen. https://elib.dlr.de/193399/

[45] Lim, B., Mahfoud, M., Das, P.T., Jeon, T., Jeon, C., Kim, M., *et al.* (2022) Advances and Key Technologies in Magnetoresistive Sensors with High Thermal Stabilities and Low Field Detectivities. *APL Materials*, **10**, Article ID: 051108. https://doi.org/10.1063/5.0087311

[46] Coramik, M., Citak, H., Ege, Y., Bicakci, S. and Gunes, H. (2023) Determining the Effect of Velocity on Sensor Selection and Position in Non-Destructive Testing with Magnetic Flux Leakage Method: A Pipe Inspection Gauge Design Study with ANSYS Maxwell. *IEEE Transactions on Instrumentation and Measurement*, **72**, 1-12. https://doi.org/10.1109/tim.2023.3284023

[47] Citak, H., Ege, Y., Bicakci, S., Gunes, H. and Coramik, M. (2020) The Determination of Buried Magnetic Material from Various Heights: A Neural Network Application. *IEEE Transactions on Instrumentation and Measurement*, **69**, 4188-4199. https://doi.org/10.1109/tim.2019.2943988

[48] Citak, H. (2020) Pulse Induction Metal Detector: A Performance Application. *IEEE Transactions on Plasma Science*, **48**, 2210-2223. https://doi.org/10.1109/tps.2020.2996182

[49] Mușuroi, C., Oproiu, M., Volmer, M. and Firastrau, I. (2020) High Sensitivity Differential Giant Magnetoresistance (GMR) Based Sensor for Non-Contacting DC/AC

Current Measurement. *Sensors*, **20**, Article 323. https://doi.org/10.3390/s20010323

[50] Wu, R., Zhang, H., Yang, R., Chen, W. and Chen, G. (2021) Nondestructive Testing for Corrosion Evaluation of Metal under Coating. *Journal of Sensors*, **2021**, Article ID: 6640406. https://doi.org/10.1155/2021/6640406

[51] Musuroi, C., Volmer, M. and Helerea, E. (2025) Improving Characteristics of Magnetoresistive Sensors for Non-Contacting Current Measurement and Low Field Sensing. 2025 *International Aegean Conference on Electrical Machines and Power Electronics* (*ACEMP*) & 2025 *International Conference on Optimization of Electrical and Electronic Equipment* (*OPTIM*), Timisoara, 14-17 May 2025, 1-10. https://doi.org/10.1109/optim-acemp62776.2025.11075245

[52] NXP Semiconductors (2020) KMZ80 Programmable AMR Angle Sensor Datasheet. https://www.nxp.com/docs/en/data-sheet/KMZ80.pdf

[53] Caruso, M.J., Bratland, T., Smith, C.H. and Schneider, R. (1998) A New Perspective on Magnetic Field Sensing. https://www.seraphim.com.tw/manager_admin/upload_file/seraphim/485/15615174851.pdf

[54] Honeywell (2010) HMC1001/HMC1002 Magnetic Sensor Datasheet. https://octopart.com/datasheet/honeywell/HMC1001-RC

[55] Honeywell (2011) HMC1051/HMC1052L/HMC1053 Magnetic Sensor Datasheet. https://octopart.com/datasheet/honeywell/HMC1052L-TR

[56] Kurlyandskaya, G.V. (2025) Challenges and Future Trends of Magnetic Sensors. MDPI. https://doi.org/10.3390/books978-3-7258-3928-5

[57] Qu, Y., Zhang, H., Zhao, R., Fu, L. and Zhou, J. (2021) Study on Working Stress Measurement Method for Steel Bars inside RC Bridges Based on Self-Magnetic Flux Leakage Spatial Signals. *Measurement*, **178**, Article ID: 109371. https://doi.org/10.1016/j.measurement.2021.109371

[58] Stamou, G., Angelopoulos, S., Ktena, A. and Hristoforou, E. (2024) 3D Anisotropic Magnetoresistance Sensor for Steel Health Monitoring. *Engineering Failure Analysis*, **160**, Article ID: 108165. https://doi.org/10.1016/j.engfailanal.2024.108165